Progress In Electromagnetics Research, Vol. 156, 63–82, 2016

The Modern High Frequency Methods for Solving Electromagnetic Scattering Problems

Yu Mao Wu[1] and Weng Cho Chew[2, *]

(*Invited Paper*)

Abstract—The high frequency scattering problems of electromagnetic fields scattered from electrically large scatterers are important and challenging. On the calculation of the reflected and diffracted wave fields, the high frequency methods could be classified into the current based method and the ray based method. In this paper, first, we give a review on the progress of the modern high frequency methods for solving the electromagnetic scattering problems. Next, due to the highly oscillatory property of the high frequency electromagnetic scattered fields, we propose the numerical steepest descent path method. Finally, we comprehensively address the high frequency wave physics, including the high frequency critical point contributions, the Keller's cone, the shadow and reflection boundaries and the creeping wave fields.

1. INTRODUCTION

Maxwell's equations are a set of four equations expressed in the integral or differential forms. Maxwell's equations were developed by Maxwell [1] early in 1865 and further simplified by Heaviside [2]. Maxwell's equations describe the interactions of the electric and magnetic fields with the external electric charge and current, which play an important role in microwave, microelectronic, quantum electrodynamics, subsurface sensing technologies, etc. [3–11].

For electromagnetic field scattered from the complicated scatterers or propagating in the complex medium, the simulation of electromagnetic field with high accuracy and speed is an important goal for the computational electromagnetic (CEM) community. Therefore, efficient methods have being developed to simulate the electromagnetic field. These methods are the method of moment (MOM) [12], the finite element method (FEM) [13], and the finite difference time domain (FDTD) method [14]. However, the analysis of the electromagnetic fields scattered from the electrically large object remains as an important and challenging problem [15]. The reason is that the computational effort for the scattered field increases vastly with the growth of the electrical size of the considered scatterer. The fast multilevel fast multipole algorithm (MLFMA) [15] reduces the workload to $O(N \log N)$, with N as the number of unknowns from the integral equation system. However, in the high frequency regime, the computational workload is still too high to afford. Hence, a fast algorithm to calculate the high frequency scattered field with acceptable workload is in great need [16].

When the frequency becomes extremely high, the electromagnetic fields assume the ray physics phenomenon. In the ray physics regime, the high frequency methods could be classified into the current based method and the ray based method. In this situation, researchers have been seeking various high

Received 2 November 2015, Accepted 26 May 2016, Scheduled 20 June 2016
Invited paper for the Commemorative Collection on the 150-Year Anniversary of Maxwell's Equations.
* Corresponding author: Weng Cho Chew (w-chew@uiuc.edu).
[1] Key Laboratory for Information Science of Electromagnetic Waves, School of Information Science and Technology, Fudan University, Shanghai 200433, China. [2] Department of Electrical and Computer Engineering, University of Illinois at Urbana-Champaign (on part-time appointment with HKU), Urbana, IL 61801, USA.

frequency methods to calculate the scattered fields over the last several decades. For the current based method, the physical optics (PO) method [17], the physical theory of diffraction (PTD) method [18, 19] and the incremental length diffraction coefficients (ILDC) method [20–23] were developed to calculate the reflected and diffracted fields with different mathematical techniques. For the ray based method, the geometric optics (GO) method, the geometric theory of diffraction (GTD) [24, 25], the uniform theory of diffraction (UTD) [26] and the uniform asymptotic theory (UAT) [27] were proposed to calculate the reflected and diffracted fields. In the high frequency regime, due to the highly localized phenomenon, the dominant contributions of the scatterer mainly come from important critical points, namely, the specular reflection point, the edge and the vertex points [28–32]. Furthermore, the specular reflection contribution from the scatterer is the leading term and the contributions from the edges and the vertices are weaker terms. To study the high frequency edge physics, the canonical solutions such as for the Sommerfeld half plane could be adopted [33]. Then, the shadow and reflection boundaries, and the Fresnel transition function for the scattered wave fields occur. For the convex scatterer and curved edges, the Fock current and the creeping wave fields occur [34]. The creeping wave field comes from the Fock current on the shadow region of the convex scatterer that creeps around the convex scatterer, which is a surface wave and decays fast as it travels along the convex surface [34, 52]. Furthermore, the ray optics approximations break down near the shadow boundary and near the caustics. Therefore, uniform solutions via the uniform approximation technique are in great need for calculating the solutions in this regime [26, 27]. Based on the aforementioned physical insights, the GTD, PTD, UTD, UAT and ILDC methods were proposed with different asymptotic and mathematical techniques. Recently, there is a progress on the numerical steepest descent path (NSDP) method [44–52] to calculate the high frequency scattered fields from the PO and ILDC methods. On invoking the NSDP method, the highly oscillatory wave fields could be transformed to smooth kernels on the complex plane. In this paper, the various high frequency methods and the fast NSDP solver will be introduced in the following.

In [53], the wave boundary element methods were proposed to calculate the high frequency wave scattering problems. Compared with the conventional direct collocation element methods, the wave boundary element methods demonstrated their high efficiencies for solving the wave scattering problems. In [54], rapidly oscillating phenomena occurring in electromagnetics, quantum theory, acoustics, fluid dynamics, electrodynamics and plasma transport, were introduced in detail. Then, the highly oscillatory quadratures were studied, like the asymptotics method, the Filon method, the Levin collocation method, the steepest descent path method. In [54, 55], the boundary integral methods adopted for solving the high frequency scattering problems were comprehensively studied. The recent progress on the analysis and implementation of numerical-asymptotic hybridization of the boundary integral methods for the acoustic scattering problems was systemically given. In [56], the wideband fast multipole method for solving the Helmholtz equation in three dimensions was studied. In the high frequency regime, on invoking the fast multipole method, the computational workload is $O(N \log N)$. In [57], the integral equations, high-order integration, fast fourier transforms and highly accurate high-frequency integrators, were studied and proposed to calculate the high frequency scattering solutions of electromagnetic and acoustic.

In [58, 59], the method of equivalent currents (MEC) was derived by the asymptotics of the surface radiation integral of the physical theory of diffraction method. And the surface radiation integral was obtained from the exact solutions of the canonical wedge problem. In [60, 61], time-domain based simulations high frequency methods were studied. In [60], the time domain uniform geometrical theory of diffraction was developed to calculate the radiation fields from elemental pulsed antennas placed on a smooth perfectly conducting convex surface. The time domain uniform geometrical theory of diffraction was further obtained by the analytic time transform technique. In [61], the time domain physical optics approximation extended the concept of the frequency-domain physical optics approximation, and used to determine some significant properties of electrically large reflector antennas with high efficiency. In [61], a time domain version of the equivalent edge current formulation of the physical theory of diffraction was derived. The time domain equivalent edge currents were expressed as the integrals of the time-domain fringe wave currents on the canonical wedge.

Compared to the work in [47–50], in this review paper, we introduced the NSDP solver to calculate the high frequency scattered fields. The NSDP method provides an efficient way to calculate the scattered field from both the PO and the ILDC techniques. The PO scattered fields could be represented

as the surface integrals, while the diffracted wave fields from the ILDC technique could be represented as line integrals. Moreover, both the PO scattered fields and the diffracted wave fields from the ILDC method are highly oscillatory with the growth of wave frequency. In this situation, we propose the NSDP method to calculate both the PO scattered fields and the diffracted wave fields. Moreover, the NSDP method could be adopted to calculate these highly oscillatory wave fields with the frequency independent computational workload and error controllable accuracy. Hence, the NSDP method may provide an efficient way to calculate the high frequency highly oscillatory wave fields from various current based high frequency methods.

This paper is organized as follows. Section 2 introduces the GO method and the ray tube technique. In Section 3, the key points of the SBR method are discussed. Section 4 addresses the key ideas of the GTD and UTD methods. Sections 5–6 illustrate the current based PO and PTD method with the radiation integrals involved. Section 7 derives the ILDC method for calculating the scattered fields from the convex body and wedge. Section 8 introduces the fast solver, namely, the NSDP method, to calculate the high frequency scattered fields from electrically large scatterers. In Section 9, the connections and comparisons of different high frequency methods are discussed. The numerical examples via the NSDP method are given in Section 10. Section 11 ends the paper with conclusions and future research areas.

2. GEOMETRIC OPTICS METHOD

In the high frequency regime, the electromagnetic fields take on the ray physics phenomenon, which are demonstrated in Figure 1(a). The incident and reflected fields could be expanded in terms of the Luneberg-Kline series as [35]

$$\mathbf{E}(\mathbf{r}) = e^{ik\psi(\mathbf{r})} \sum_{j=0}^{\infty} \frac{\mathbf{E}_j(\mathbf{r})}{(-i\omega)^j} \tag{1}$$

In this paper, the time dependence $e^{-i\omega t}$ is assumed. And $\mathbf{r}$ is the position point in spatial space; k and ω are the wavenumber and the angular velocity of the background medium; $\psi(\mathbf{r})$ is the wave front surface at the position point $\mathbf{r}$; $\mathbf{E}_j(\mathbf{r})$ is independent of wave frequency. Furthermore, the light intensity between any two points in space follows the ray tube theory. That is, the conservation of energy flux follows along the ray path, as shown in Figure 2(a). Furthermore, by adopting the ray tube technique, the leading term in Equation (1) could be obtained as [29]

$$\mathbf{E}(\mathbf{r}) \approx \mathbf{E}_0(\mathbf{r}_0) \sqrt{\frac{\rho_1 \rho_2}{(\rho_1 + l)(\rho_2 + l)}} e^{ikl} \tag{2}$$

Here, $\mathbf{E}_0(\mathbf{r}_0)$ follows the leading term of Equation (1) at $\mathbf{r}_0$. ρ_1 and ρ_2 are the principal radii of the wavefront curvature with respect to the reference point $\mathbf{r}_0$, and

$$l = \|\mathbf{r} - \mathbf{r}_0\|_2 \tag{3}$$

denotes the distance between the reference point $\mathbf{r}_0$ and the position point $\mathbf{r}$, which is demonstrated in Figure 1(a).

Importantly, the ray path between any two points $\mathbf{r}_1$ and $\mathbf{r}_2$ in space follows the Fermat's principle, which is governed by

$$\delta \int_{\mathbf{r}_1}^{\mathbf{r}_2} n(s) ds = 0 \tag{4}$$

Here, $n(s)$ represents the refraction index of the medium, and δ is the variation operator. In physics, Equation (4) means that the ray propagates along the path that minimizes the optical distances between any two points in space. Then, on invoking the Fermat's principle in Equation (4), the direction of the reflected rays could be determined from the incident ray in Figure 2(b).

Based on the ray tubes theory and the Fermat's principle, the reflected field $\mathbf{E}^{(r)}(\mathbf{r})$ at distance l from the reflection point $\mathbf{p}_r$ of the considered scatterer could be expressed as

$$\mathbf{E}^{(r)}(\mathbf{r}) \approx \overline{\mathbf{R}} \cdot \mathbf{E}^{(i)}(\mathbf{p}_r) \sqrt{\frac{\rho_1(\mathbf{p}_r)\rho_2(\mathbf{p}_r)}{(\rho_1(\mathbf{p}_r) + l)(\rho_2(\mathbf{p}_r) + l)}} e^{ikl} \tag{5}$$

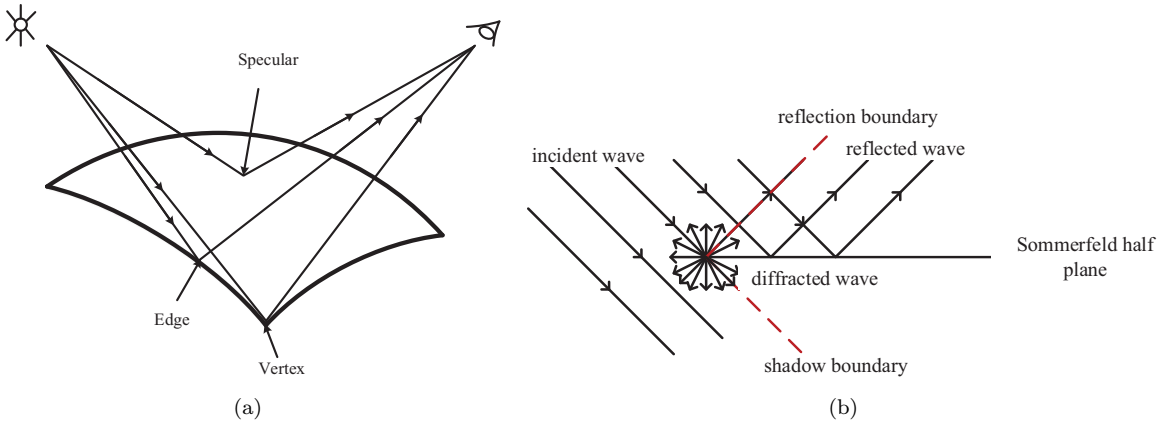

Figure 1. (a) High frequency ray fields from the scatterer, including the reflected fields from the spatial specular points and the diffracted fields from the edge points and the vertex points. (b) The wave physics of the Sommerfeld half plane problem.

Here, $\overline{\mathbf{R}}$ is the dyadic reflection coefficient from $\mathbf{p}_r$, and $\mathbf{E}^{(i)}(\mathbf{p}_r)$ represents the incident field at $\mathbf{p}_r$. And $\rho_1(\mathbf{p}_r)$ and $\rho_2(\mathbf{p}_r)$ are the principle radii of $\partial\Omega$ at $\mathbf{p}_r$, and l is the distance from $\mathbf{p}_r$ to $\mathbf{r}$ along the direction of the reflected field. Furthermore, the term $\sqrt{\frac{\rho_1(\mathbf{p}_r)\rho_2(\mathbf{p}_r)}{(\rho_1(\mathbf{p}_r)+l)(\rho_2(\mathbf{p}_r)+l)}}$ in Equation (5) represents the spatial attenuation factor. The dyadic reflection coefficient $\overline{\mathbf{R}}$ depends on the local curvature and the material property of the scatterer. In particular, for the perfectly conducting (PEC) scatterer, one has

$$\overline{\mathbf{R}} = \begin{bmatrix} 1 & 0 \\ 0 & -1 \end{bmatrix} \tag{6}$$

Hence, when the observation point $\mathbf{r}$ is located at the reflection point $\mathbf{p}_r$ of the PEC scatterer, we have

$$\mathbf{E}^{(r)}(\mathbf{p}_r) \approx \overline{\mathbf{R}} \cdot \mathbf{E}^{(i)}(\mathbf{p}_r) = \mathbf{E}^{(i)}(\mathbf{p}_r) \cdot \left(\hat{e}^i_{\parallel}\hat{e}^r_{\parallel} - \hat{e}^i_{\perp}\hat{e}^r_{\perp}\right) \tag{7}$$

Here, $\hat{e}^i_{\parallel}$ and $\hat{e}^i_{\perp}$ correspond to the unit vectors that are parallel and perpendicular to the plane of incidence, and $\hat{e}^r_{\parallel}$ and $\hat{e}^r_{\perp}$ follow the similar definition for the reflected wave fields, which are formulated as

$$\hat{e}^i_{\perp} \times \hat{k}^i = \hat{e}^i_{\parallel} \tag{8}$$

$$\hat{e}^r_{\perp} \times \hat{k}^r = \hat{e}^r_{\parallel} \tag{9}$$

and demonstrated in Figure 2(b).

The GO method provides a fast way to calculate the reflected field from the electrically large scatterer as given in Equation (5). From Equation (5), it is evident that the workload of calculating the reflected field via the GO method could be achieved frequency independently.

3. SHOOTING AND BOUNCING RAY METHOD

For the external source incident on the complicated structure like the cavity in Figure 3, because of the multiple reflection and diffraction, the ray physics is rather complicated. In particular, the rapid variation of the curvature of the cavity, large dimension of the cavity and inhomogeneous medium of the cavity make the simulation of high frequency wave fields challenging.

In 1989, Ling et al. [36] proposed the shooting and bouncing ray (SBR) method to capture the scattered fields from the cavity. The SBR method contains three parts. The first part is the ray tracing technique. That is, for the considered scatterer and the incident wave, one finds the multiple ray paths from the Snell's law and the Fermat's principle, which is given in Equation (4).

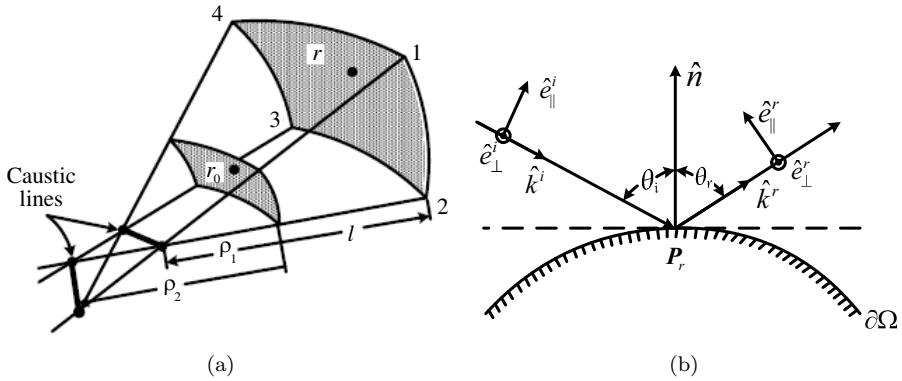

Figure 2. (a) The ray tube figure in [29]. (b) Reflection of the incident rays from the scatterer in [29].

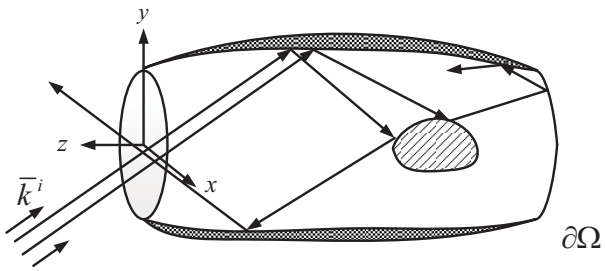

Figure 3. The multiple reflections from the cavity in [36].

The second part is the determination of the amplitude of the exit rays based on the amplitude tracking, which is formulated as

$$\mathbf{E}(\mathbf{r}_{j+1}) = (\overline{\mathbf{R}})_j \cdot \mathbf{E}(\mathbf{r}_j)(DF)_j e^{ik\|\mathbf{r}_{j+1}-\mathbf{r}_j\|_2}, \quad j = 1, 2, \cdots, N. \tag{10}$$

Here, $\mathbf{r}_j$ are the sampling points on the cavity. And $\overline{\mathbf{R}}_j$ is the dyadic reflection coefficient matrix at the reflection point $\mathbf{r}_j$ with the local tangent plane approximation technique, which is demonstrated in Figure 3. The factor $(DF)_j$ is the amplitude divergence factor after the j-th reflection and before the $(j+1)$-th reflection with the ray tube technique. And $k\|\mathbf{r}_{j+1} - \mathbf{r}_j\|$ corresponds to the phase factor traveling from the point $\mathbf{r}_j$ to $\mathbf{r}_{j+1}$ along the ray path.

The final part of the SBR method is the application of the physical optics (PO) method to calculate the scattered fields and the radar cross section (RCS) from the cavity structure. With the ray tube technique, the calculation of the PO scattered fields could be further reduced to the calculation of the following integral

$$I = \int_{\Delta} dydx e^{ik(ax+by)} \tag{11}$$

Here, a and b are constants depending on the information of the incident wave fields and the ray tube. Furthermore, the integral I in Equation (11) could be evaluated analytically by the Fourier transformation technique [37]. One could notice that Equation (11) contains the linear phase term, and the dense sampling mesh with size of $\lambda/10$ is required. Hence, the computational workload for the scattered fields via the SBR method shall increase vastly with the increase of the external wave frequency.

4. GEOMETRIC THEORY OF DIFFRACTION AND UNIFORM THEORY OF DIFFRACTION

As discussed in Section 2, the GO method could be used to evaluate the reflected fields. However, when the rays come to the wedges and the convex scatterers, the diffracted wave fields emerge. In this

situation, when the observation point lies in the deep shadow regions, the GO method fails to capture the scattered wave fields very well [24].

In 1896, Sommerfeld [33] addressed the early high frequency scattering problem from the perfect conducting half plane, as shown in Figure 1(b). The scattered field was given in a closed form, which was expressed in terms of the Fresnel integral [33]. With the asymptotic expansion of the Fresnel integral, the scattered far field could be captured in an elegant way. The high frequency diffracted wave physics such as the fringe current, shadow and reflection boundaries were clearly demonstrated. The regions for the observation point lying around the reflection and shadow boundaries are named as transition regions.

The calculation of the diffracted ray fields from the perfectly conducting curved wedges was given by Keller [24]. This method was called the geometric theory of diffraction (GTD) method. In detail, after solving the diffracted fields from the canonical wedge and adopting the ray tube technique, the leading term of the diffracted wave fields from the point $\mathbf{p}_d$ along the curved wedge has a similar formulation to that given in Equation (5) [24]:

$$\mathbf{E}^{(d)}(\mathbf{r}) \approx \mathbf{E}^{(i)}(\mathbf{p}_d) \cdot \overline{\mathbf{D}} \sqrt{\frac{\rho_d(\mathbf{p}_d)}{l(\rho_d(\mathbf{p}_d)+l)}} e^{ikl} \tag{12}$$

In Equation (12), $\overline{\mathbf{D}}$ is the dyadic diffraction coefficient in [24], and l denotes the distance between the two points $\mathbf{r}$ and $\mathbf{p}_d$. And $\rho_d(\mathbf{p}_d)$ denotes the distance of the edge and the second caustic of the diffracted ray. In Figure 4, we demonstrate the figure of the diffraction from the curved edge with

$$\hat{\phi}^i = \hat{\mathbf{r}}^i \times \hat{\theta}^i \tag{13}$$

$$\hat{\phi}^d = \hat{\mathbf{r}}^d \times \hat{\theta}^d \tag{14}$$

that is, the diffracted ray $(r^d, \pi - \phi^d, \theta^d)$ and incident ray $(r^i, \pi - \phi^i, \theta^i)$ are represented in the spherical coordinate system. The unit vectors $\hat{r}^i$ and $\hat{r}^d$ are in the directions of the incidence and diffraction rays at the edge, respectively. The unit vectors $\hat{\phi}^i$ and $\hat{\phi}^d$ are parallel to the edge fixed plane of incidence and diffraction. The unit vectors $\hat{\theta}^i$ and $\hat{\theta}^d$ are perpendicular to the edge fixed plane of incidence and diffraction.

For the diffraction of the PEC wedge, similar to that given in Equation (12), the relationship between the incident field and the diffracted field could be formulated as

$$\mathbf{E}^{(d)}(\mathbf{r}) \approx \mathbf{E}^{(i)}(\mathbf{p}_d) \cdot \overline{\mathbf{D}} A(l', l) e^{ikl} \tag{15}$$

where $A(l', l)$ corresponds to the attenuation factor of the amplitude of $\mathbf{E}^{(d)}(\mathbf{r})$ along the diffracted rays. Here, l' denotes the distance of the source point and the diffraction point $\mathbf{p}_d$, and l denotes the distance of the diffraction point $\mathbf{p}_d$ and the observation point $\mathbf{r}$. For the plane and conical incident waves, $A(l', l)$ takes the formulation [26]

$$A(l', l) = \frac{1}{\sqrt{l}} \tag{16}$$

While for the spherical incident wave, $A(l', l)$ takes the form

$$A(l', l) = \sqrt{\frac{l'}{l(l'+l)}} \tag{17}$$

The diffraction coefficient $\overline{\mathbf{D}}$ could be obtained from the asymptotic expansion of the radiation integrals for the canonical PEC wedge diffraction problem. Hence, the fields from the GTD method contain both the fields from the GO method and the diffracted wave fields, which are more accurate for calculating the high frequency wave fields. Moreover, the dyadic diffraction coefficient $\overline{\mathbf{D}}$ takes the form

$$\overline{\mathbf{D}} = -\hat{\phi}_i \hat{\phi}_d D_s - \hat{\theta}_i \hat{\theta}_d D_h \tag{18}$$

where D_s and D_h correspond to the scalar diffraction coefficients for the two dimensional canonical wedge diffraction problems with the Dirichlet and Neumann boundary conditions [24], respectively.

Keller gave the scalar diffraction coefficients as [24]

$$D_{s,h}(\theta_d,\theta_i;\phi_i)=\frac{e^{i\frac{\pi}{4}}\sin\dfrac{\pi}{n}}{n\sqrt{2\pi k}\sin\phi_i}\chi(n,\theta_i,\theta_d) \tag{19}$$

where

$$\chi(n,\theta_i,\theta_d)=\frac{1}{\cos\pi/n-\cos[(\theta_i-\theta_d)/n]}\mp\frac{1}{\cos\pi/n-\cos[(\theta_i+\theta_d)/n]}$$

Here, the wedge takes the angle $(2-n)\pi$. The "$\mp$" sign corresponds to the Dirichlet and Neumann boundary conditions for the PEC wedge diffraction problems. When the observation point $\mathbf{r}$ lies near the reflection and incident shadow boundaries with $\theta_d=\pi\mp\theta_i$, the above Equation (19) breaks down. Furthermore, from Equations (15) and (19), we see that the diffracted wave fields $\mathbf{E}^{(d)}(\mathbf{r})$ is $O\left(\frac{1}{\sqrt{k}}\right)$. In Equation (5), the reflected fields are $O(1)$. Hence, when the wave frequency goes large, the reflected field becomes more important than the diffracted field. In this sense, the GO method will become more accurate with the increase of wave frequency. In particular, when $n=2$, the above problem reduces to the so-called Sommerfeld half plane problem.

To solve the above break down problems around the incident and reflection shadow boundaries in [24], the scattered fields from the canonical PEC wedge are expressed in terms of the contour integrals on the complex plane. The uniform asymptotic technique, named as Pauli-Clemmow modified method of steepest descent, was adopted to evaluate these contour integrals by Kouyoumjian and Pathak [26]. Then, the dyadic diffraction coefficient of a PEC wedge was obtained as [26]

$$D_{s,h}(\theta_d,\theta_i;\phi_i)=-\frac{e^{i\frac{\pi}{4}}}{2n\sqrt{2\pi k}\sin\phi_i}X(n,\theta_d,\theta_i) \tag{20}$$

$$\begin{aligned}X(n,\theta_d,\theta_i)&=\cot\left(\frac{\pi+(\theta_d-\theta_i)}{2n}\right)F\left[kDa^+(\theta_d-\theta_i)\right]\\&+\cot\left(\frac{\pi-(\theta_d-\theta_i)}{2n}\right)F\left[kDa^-(\theta_d-\theta_i)\right]\\&\mp\cot\left(\frac{\pi+(\theta_d+\theta_i)}{2n}\right)F\left[kDa^+(\theta_d+\theta_i)\right]\\&\mp\cot\left(\frac{\pi-(\theta_d+\theta_i)}{2n}\right)F\left[kDa^-(\theta_d+\theta_i)\right]\end{aligned} \tag{21}$$

In the above Equation (21), $F(x)$ involves the Fresnel function [42]

$$F(x)=-2i\sqrt{x}e^{-ix}\int_{\sqrt{x}}^{\infty}e^{i\tau^2}d\tau \tag{22}$$

The parameters $a^{\pm}(x)$ and D are related to the incident wave fields information, which were given in [26]. The formulation in Equation (20) for calculating the diffracted wave fields is named as uniform theory of diffraction (UTD) [26]. When the observation points lie around the incident and reflection shadow boundaries, one could analyze that Equation (21) is finite by the asymptotic expansion of $F(x)$ [26]. Hence, $D_{s,h}(\theta_d,\theta_i;\phi_i)$ in Equation (20) is finite. In this situation, the UTD method could overcome the break down problem in the GTD method.

5. PHYSICAL OPTICS METHOD

In 1913, Macdonald introduced the physical optics (PO) approximation method by approximating the induced current on the surface of the scatterer [17]. The PO approximation serves as an efficient technique to calculate the scattered fields from the electrically large and smooth scatterers [37, 38]. Specifically, for the external source impinging on the considered scatterer, in the lit region, the PO induced current is approximated with the local tangent plane approximation, which is usually good

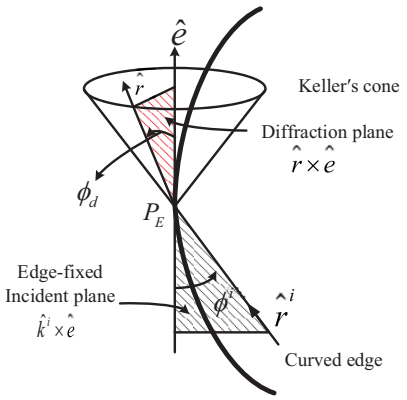

Figure 4. The diffraction from the curved wedge with the Keller's cone geometry in [29].

for the locally flat and smooth surface of the scatterer. On the other hand, in the shadow region, the PO induced current is set to be zero. However, the PO current is not correct around the shadow boundary [18], which leads to the fact that the PO method does not satisfy the reciprocity theorem. The induced current in the lit region of the scatterer could be approximated as

$$\mathbf{J}_{PO}(\mathbf{r}) = 2\hat{n}(\mathbf{r}) \times \mathbf{H}^{(i)}(\mathbf{r}) \tag{23}$$

Equation (23) is known as the PO current, which is demonstrated in Figure 5. Here, $\hat{n}(\mathbf{r})$ is the outward unit normal to the surface, and $\mathbf{H}^{(i)}(\mathbf{r})$ is the incident source field. Then, the electric scattered far fields from the PO current could be expressed as

$$\mathbf{E}^{(s)}(\mathbf{r}) \approx \frac{ike^{ikr}}{4\pi r}\sqrt{\frac{\mu}{\epsilon}}\left(\overline{\mathbf{I}} - \hat{r}\hat{r}\right) \cdot \int_{\partial\Omega_1} d\mathbf{r}' e^{-ik\hat{r}\cdot\mathbf{r}'}\mathbf{J}_{PO}(\mathbf{r}') \tag{24}$$

In particular, for the plane incident wave, one has

$$\mathbf{E}^{(i)}(\mathbf{r}) = \mathbf{E}_0{}^{(i)} e^{ik\hat{\mathbf{r}}^{(i)}\cdot\mathbf{r}}, \quad \mathbf{H}^{(i)}(\mathbf{r}) = \frac{\hat{\mathbf{r}}^{(i)} \times \mathbf{E}_0{}^{(i)}}{Z_0} e^{ik\hat{\mathbf{r}}^{(i)}\cdot\mathbf{r}} \tag{25}$$

with Z_0 as the intrinsic impedance of free space. In this situation, the scattered electric field could be rewritten as

$$\mathbf{E}^{(s)}(\mathbf{r}) \approx \int_{\partial\Omega_1} \mathbf{s}(\mathbf{r}') e^{ikv(\mathbf{r}')} dS(\mathbf{r}') \tag{26}$$

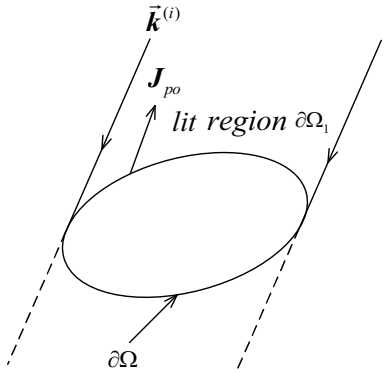

Figure 5. PO approximation current on the PEC scatterer.

with

$$\mathbf{s}(\mathbf{r}') = -\frac{ike^{ikr}}{2\pi r}\hat{\mathbf{r}} \times \hat{\mathbf{r}} \times \left(\hat{\mathbf{n}}(\mathbf{r}') \times \hat{\mathbf{r}}^{(i)} \times \mathbf{E}_0{}^{(i)}\right) \tag{27}$$

$$v(\mathbf{r}') = \left(\hat{\mathbf{r}}^{(i)} - \hat{\mathbf{r}}\right) \cdot \mathbf{r}' \tag{28}$$

Equation (26) is the bistatic scattered electric field under the PO approximation. The vector function $\mathbf{s}(\mathbf{r}')$ in Equation (27) is known as the vector amplitude function, and $v(\mathbf{r}')$ in Equation (28) is the phase function. The integrand of the vector PO surface integral in Equation (26) is highly oscillatory when kL goes large. Here, L is the diameter of the considered scatterer. The highly oscillatory property of the PO integrand makes the computational effort grow via the direct numerical integration method. Therefore, one needs to seek efficient techniques to evaluate these PO integrals.

6. PHYSICAL THEORY OF DIFFRACTION

The limitation of the PO approximation is that the PO current fails to capture the electric current around the shadow boundary. To remedy this limitation, Ufimtsev considered the PEC wedge diffraction problems, which is shown in Figure 6. He introduced the edge current to correct the PO current, known as the physical theory of diffraction (PTD) method [19]. In mathematics, the PTD current takes the expression

$$\mathbf{J}_{PTD}(\mathbf{r}) = \mathbf{J}_{PO}(\mathbf{r}) + \mathbf{J}_{NU}(\mathbf{r}) \tag{29}$$

where $\mathbf{J}_{NU}(\mathbf{r})$ is the edge current used to correct the limited accuracy of $\mathbf{J}_{PO}(\mathbf{r})$ around the shadow boundary and in the deep shadow regions. Similar to the GTD problem introduced in Section 4, the non-uniform (NU) current $\mathbf{J}_{NU}(\mathbf{r})$ could also be obtained from the canonical PEC wedge diffraction problem. After substituting $\mathbf{J}_{PTD}(\mathbf{r})$ in Equation (29) into (24), one could obtain the scattered far fields from the PTD method, with the formulation

$$\mathbf{E}^{(s)}(\mathbf{r}) \approx \frac{ike^{ikr}}{4\pi r}\sqrt{\frac{\mu}{\epsilon}}\left(\overline{\mathbf{I}} - \hat{r}\hat{r}\right) \cdot \int_{\Omega} d\mathbf{r}' e^{-ik\hat{r}\cdot\mathbf{r}'}\mathbf{J}_{PTD}(\mathbf{r}') \tag{30}$$

The differences of the PTD scattered fields and the PO scattered fields lie in two parts. First, instead of the lit region $\partial\Omega_1$ of the scatterer in Equation (24), one could see that the integration domain in Equation (30) is $\partial\Omega$. Second, the resultant scattered fields contain the PO scattered field in Equation (30) and the edge diffracted wave field, which is also regarded as the radiation integral with highly oscillatory integrand. Meanwhile, with the consideration of the computational workload, it is frequency dependent to evaluate the radiation integral from the PTD method by the direct numerical integration scheme.

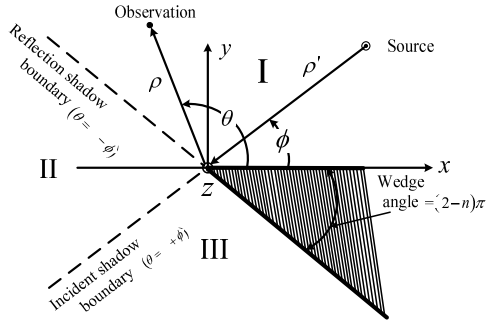

Figure 6. The diffraction from the PEC wedge.

7. INCREMENTAL LENGTH DIFFRACTION COEFFICIENT TECHNIQUE

The incremental length diffraction coefficient (ILDC) technique, which was proposed by Mitzner early in 1974, was used to calculate the diffracted wave fields from the wedge diffraction problem [20]. Latter,

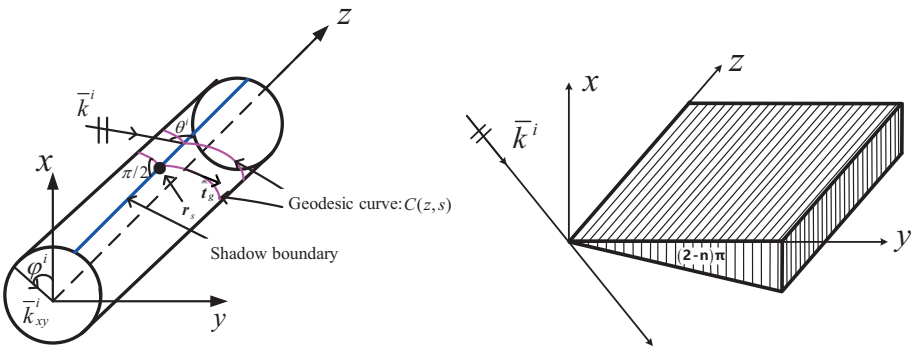

Figure 7. (a) The obliquely incident plane wave with wavevector $\mathbf{k}^i$ that impinges on the convex cylinder with finite length; the shadow boundary is shown by the blue line on the cylinder. The shadow boundary point $\mathbf{r}_s$ is denoted by the black dot on the shadow boundary. (b) The geometry of the finite length wedge diffraction from the obliquely incident wave.

Yaghjian and Shore [21–23] comprehensively studied the ILDC technique, and further extended the ILDC technique to the convex scatterer. Recently, Wu and Chew [52] proposed the numerical contour deformation technique together with the ILDC technique to evaluate the diffracted wave fields from the three dimensional convex scatterer. The details of the ILDC technique are introduced as follows.

In Figure 7, we define the integration surface from the scatterer (the cylinder or the wedge) as [52]

$$\Omega(x,y,z) = C(x,y) \times [z_a, z_b] \tag{31}$$

Here, $C(x,y)$ is the cross section of the contour curve on the x-y plane, and $[z_a, z_b]$ is the integration domain along the z-axis. Then, on performing the integration of the free space dyadic Green's function and the uniform current over $\partial\Omega(x,y,z)$, we have

$$\mathbf{E}^{(s,q)}(\mathbf{r}) = i\omega\mu\left(\mathbf{I} + \frac{\nabla\nabla}{k^2}\right) \cdot \int_{\partial\Omega} d\mathbf{r}' \frac{\mathbf{K}^{(q)}(\hat{\mathbf{r}}^i, \mathbf{r}')e^{ik|\mathbf{r}-\mathbf{r}'|}}{4\pi|\mathbf{r}-\mathbf{r}'|} \tag{32}$$

Here, $\mathbf{K}^{(q)}(\hat{\mathbf{r}}^i, \mathbf{r}')$ represents the uniform current for the cylinder or the wedge, named as the Fock or the fringe current [21, 23, 52], respectively. Index q corresponds to the TE and TM cases. For notational convenience, we omit index q in the rest of this paper. In the far field approximation, Equation (32) could be formulated as

$$\mathbf{E}^{(s)}(\mathbf{r}) \approx \frac{ike^{ikr}}{4\pi r}\sqrt{\frac{\mu}{\epsilon}}\left(\hat{\theta}\hat{\theta} + \hat{\phi}\hat{\phi}\right) \cdot \int_{\partial\Omega} d\mathbf{r}' e^{-ik\hat{\mathbf{r}}\cdot\mathbf{r}'}\mathbf{K}\left(\hat{\mathbf{r}}^i, \mathbf{r}'\right) \tag{33}$$

To adopt the ILDC technique, we consider the differential formulation of $\Omega(x,y,z)$ with respect to the z-axis, which is given by $d\Omega(x,y,z) = \widetilde{C}(s) \times dz$. Here, $\widetilde{C}(s)$ is the parameterization of contour $C(x,y)$ on the x-y plane with the parameter s. In the illuminated region, $\widetilde{C}(s)$ is normal to the shadow boundary, that is, $\widetilde{C}(s)$ follows the direction of the incident wavevector $\hat{\mathbf{k}}^i$. In the shadow region, $\widetilde{C}(s)$ is the geodesic curve whose tangential direction forms θ^i angle with the z-axis, as shown in Figure 7. Then, the scattered fields $d\mathbf{E}^{(s)}(\mathbf{r})$ at the observation point $\mathbf{r}$ away from the incremental current sheet of length dz could be formulated as

$$d\mathbf{E}^{(s)}(\mathbf{r}) \approx dz\frac{ike^{ikr}}{4\pi r}\sqrt{\frac{\mu}{\epsilon}}\left(\hat{\theta}\hat{\theta} + \hat{\phi}\hat{\phi}\right) \cdot \int_{\widetilde{C}(s)} d\mathbf{r}' e^{-ik\hat{\mathbf{r}}\cdot\mathbf{r}'}\mathbf{K}(\hat{\mathbf{r}}^i, \mathbf{r}') \tag{34}$$

Here, the shadow boundary curve is governed by

$$\hat{\mathbf{k}}^i \cdot \hat{\mathbf{n}}_s(\mathbf{r}_s) = 0 \tag{35}$$

where $\hat{\mathbf{n}}_s(\mathbf{r}_s)$ is the outward unit normal vector at the point $\mathbf{r}_s$ lying on the shadow boundary of the scatterer. With the observation point $\mathbf{r}$ lying in the lit and shadow regions of the considered scatterers, we have

$$\hat{\mathbf{k}}^i \cdot \hat{\mathbf{n}}(\mathbf{r}) < 0, \quad \hat{\mathbf{k}}^i \cdot \hat{\mathbf{n}}(\mathbf{r}) > 0 \tag{36}$$

respectively. On invoking the ILDC technique, we see that Equation (34) represents the incremental length scattered fields along the z direction.

By subtracting the PO current from the uniform current, we have the non-uniform (NU) incremental diffraction wave fields around the transition region of the scatterer as

$$\delta\mathbf{E}^{(s,NU)}(\mathbf{r}) \approx dz \frac{ike^{ikr}}{4\pi r}\sqrt{\frac{\mu}{\epsilon}}\left(\hat{\theta}\hat{\theta}+\hat{\phi}\hat{\phi}\right)\cdot\int_{\widetilde{C}(s)} d\mathbf{r}' e^{-ik\hat{\mathbf{r}}\cdot\mathbf{r}'}\mathbf{K}^{(NU)}(\hat{\mathbf{r}}^i,\mathbf{r}') \tag{37}$$

Here,

$$\mathbf{K}(\hat{\mathbf{r}}^i,\mathbf{r}') = \mathbf{K}^{(PO)}(\hat{\mathbf{r}}^i,\mathbf{r}') + \mathbf{K}^{(NU)}(\hat{\mathbf{r}}^i,\mathbf{r}'). \tag{38}$$

In wave physics, the term $\mathbf{K}^{(PO)}(\hat{\mathbf{r}}^i,\mathbf{r}')$ corresponds to the PO current in the scatterer's lit region, and $\mathbf{K}^{(NU)}(\hat{\mathbf{r}}^i,\mathbf{r}')$ is the NU-Fock or NU-fringe currents near the transition region and in the deep shadow region. The expression of the Fock current $\mathbf{K}^{(NU)}$ is formulated via the current on the cylinder diffraction problems and the Sommerfeld-Watson transformation technique, which involves the Airy function and its derivative [34, 52]. The fringe current follows the solution of the canonical wedge diffraction problem, which is expressed as the contour integral on the complex plane [20].

8. THE NUMERICAL STEEPEST DESCENT PATH METHOD

On invoking the high frequency asymptotic (HFA) method, the radiation integrals in Equations (26, 30) from the PO and PTD methods could be approximated as several leading terms [28, 39–41]. However, the generated high frequency scattered fields results usually lose accuracy. This limitation becomes serious when the parameter kL is not extremely large but lies in the high frequency regime.

To remedy the aforementioned limitation from the HFA method, Wu and Chew proposed the numerical steepest descent path (NSDP) method [47, 49, 50]. On invoking the NSDP method, the PO integrands are transformed to exponentially decay integrands on the complex NSDPs, which could be integrated with workload independent of frequency. With respect to the integration accuracy, the only approximation process via the NSDP method is the numerical integration of the exponentially decay PO integrand [43]. Therefore, compared to the HFA method, the proposed NSDP method could improve the accuracy of the PO scattered field .

We define the NSDP method as follows. For the given integration domain $[L_1, L_2]$ with the highly oscillatory integrand $e^{ikg(x)}$, one could define the path functions $x = x_{L_m}(p)$, $m = 1, 2$, $p \in [0, \infty)$, satisfying the following three conditions [3]:
(a) $x_{L_m}(0) = L_m$, that is, the paths start at L_m.
(b) $\mathrm{Re}(g(x_{L_m}(p))) = \mathrm{Re}(g(x_{L_m}(0))) \equiv C$, where C is a constant.
(c) Im $(g(x_{L_m}(p))) = p$.

Then, after substituting $x = x_{L_m}(p)$ into the phase function $g(x)$, one could see that $e^{ikg(x_{Lm}(p))} = e^{ikg(L_m)-kp}$ decreases exponentially as $O(e^{-kp})$. The above contour transformation technique on deforming the real integration variable "x" to the complex path function $x_{L_m}(p)$ is called the NSDP technique. Through (a), (b) and (c), the NSDPs $x_{L_m}(p)$ for the end points L_m could also be obtained [47–50].

However, one could notice that $g(x) - g(x_s)$ is a quadratic function after the Taylor expansion of $g(x)$ at x_s [3]. Hence, the behavior of $g(x)$ at x_s is different from that at the end points. This fact leads to the change of the corresponding NSDPs on the complex plane. Therefore, for the stationary phase point x_s, one needs to change the above condition (c) to $\mathrm{Im}(g(x_{L_m}(p))) = p^2$, and define the corresponding NSDP, $x = x_0(p)$, $p \in (-\infty, \infty)$.

As known in [47–50], the quadratic phase variations for the PO scattered fields in Equation (26) cover the high frequency critical points. Hence, the quadratic variation for the phase functions on

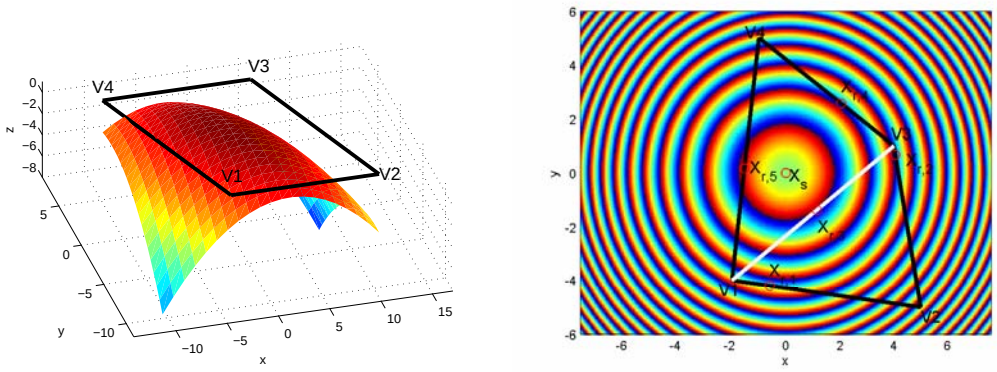

(a) (b)

Figure 8. (a) A parabolic PEC patch with formulation $f(x, y, z) : z = 1 - 0.06\left(x^2 + xy + y^2\right)$. (b) The projected x–y quadrilateral domain $\mathbf{V}_1\mathbf{V}_2\mathbf{V}_3\mathbf{V}_4$ of the parabolic PEC patch.

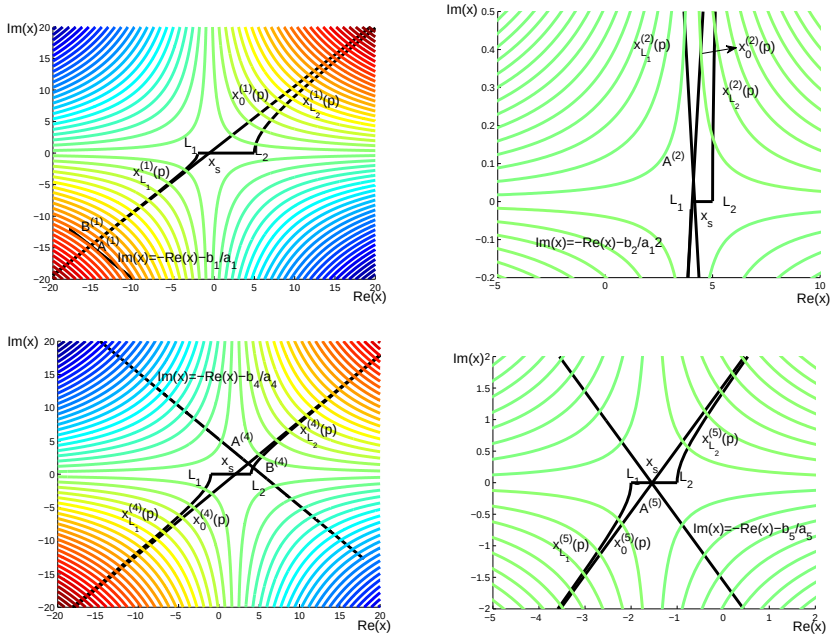

Figure 9. The four sub-figures correspond to the NSDPs for the integrands of $I_2^{(a_m,b_m)}, m = 1, 2, 4, 5$, defined on the four edges of the quadrilateral domain $\mathbf{V}_1\mathbf{V}_2\mathbf{V}_3\mathbf{V}_4$ in Figure 8.

the quadrilateral PEC patches in Figure 8 is considered [49]. The projected quadrilateral domain on the xy plane is denoted as $\mathbf{V}_1\mathbf{V}_2\mathbf{V}_3\mathbf{V}_4$. The four edges of the quadrilateral domain are governed by $y = a_m x + b_m$, $m = 1, 2, 4, 5$. Then, after substituting the parabolic patch $\partial\Omega$ in Figure 8 into Equation (24), the three PO surface integrals could be obtained. For simplicity, one can denote them as $\tilde{I}$. In the process of the reduction of the PO surface integral into several line integrals $I_2^{(a_m,b_m)}$, the complementary error function emerges in the integrand [47]. On invoking the Stokes' phenomenon of the complementary error function [42], the phase functions on the four edges are $g^{(m)}(x) = x^2 + (a_m x + b_m)^2$, and the Stokes' lines are $y = -x - \frac{b_m}{a_m}$. Then, the NSDPs on the four edges of the quadrilateral domain are [3]:

$$x_{L_m}(p) = \frac{\mathrm{sgn}(L'_m)}{\sqrt{1 + a_m^2}} \sqrt{{L'_m}^2 + ip} + x_s,\ p \in [0, \infty) \tag{39}$$

$$x_{0,m}(p) = \frac{e^{(i\frac{\pi}{4})}p}{\sqrt{1+a_m^2}} + x_s,\ p \in (-\infty, \infty) \tag{40}$$

where $x_s = -\frac{a_m b_m}{1+a_m^2}$ is the stationary phase point of the phase function $g^{(m)}(x)$ defined on the four edges, and $L'_m = \sqrt{1+a_m^2}\,(L_m - x_s)$. These NSDPs are demonstrated in Figure 9. After changing the original PO integration path to the NSDPs and on invoking the Cauchy's integral theorem, the PO integral $\tilde{I}$ can be represented in terms of the NSDPs as

$$\tilde{I} = -I_2^{(a_1,b_1)} + I_2^{(a_2,b_2)} + I_2^{(a_4,b_4)} + I_2^{(a_5,b_5)} \tag{41}$$

where

$$\begin{aligned}
I_2^{(a_1,b_1)} &= I_{L_1}^{(a_1,b_1)} - I_{L_2}^{(a_1,b_1)} + I_{x_s}^{(a_1,b_1)} \\
&\quad + K\left((\mathbf{V}_2(1),0)\right) - K\left((\mathbf{V}_1(1),0)\right) - K\left(\mathbf{B}^{(1)}\right) + K\left(\mathbf{A}^{(1)}\right) \\
I_2^{(a_2,b_2)} &= I_{L_1}^{(a_2,b_2)} + I_{x_s}^{(a_2,b_2)} - I_{L_2}^{(a_2,b_2)} + K\left((\mathbf{V}_2(1),0)\right) - K\left(\mathbf{A}^{(2)}\right) \\
I_2^{(a_4,b_4)} &= I_{L_1}^{(a_4,b_4)} + I_{x_s}^{(a_4,b_4)} - I_{L_2}^{(a_4,b_4)} + K\left(\mathbf{B}^{(4)}\right) - K\left(\mathbf{A}^{(4)}\right) \\
I_2^{(a_5,b_5)} &= I_{L_1}^{(a_5,b_5)} + I_{x_s}^{(a_5,b_5)} - I_{L_2}^{(a_5,b_5)} + K\left(\mathbf{A}^{(5)}\right) - K\left((\mathbf{V}_1(1),0)\right)
\end{aligned}$$

Originally, $I_2^{(a_m,b_m)}, m = 1,2,4,5$, are the highly oscillatory PO line integrals $I_2^{(a,b)}$ defined on the four edges $\overrightarrow{\mathbf{V}_1\mathbf{V}_2}$, $\overrightarrow{\mathbf{V}_2\mathbf{V}_3}$, $\overrightarrow{\mathbf{V}_3\mathbf{V}_4}$ and $\overrightarrow{\mathbf{V}_1\mathbf{V}_4}$ in Figure 8. Here, $K(x)$ comes from the Stokes' phenomenon of erfc(z)'s different asymptotic behaviors on different domains, which has the closed-form formula. At this point, the PO integral is expressed in terms of some NSDPs with exponentially decay integrands, which could be evaluated with frequency independent workload.

On invoking the NSDP method proposed in [47], Wu and Chew expressed the high frequency critical point contributions via the PO integrand defined on the NSDPs. Since the process for evaluating the PO integral uses less approximation, these PO integral results could gain high accuracy from those produced by the HFA method. Meanwhile, the frequency independent workload is achieved [47–50].

9. THE CONNECTIONS AND COMPARISONS OF THE HIGH FREQUENCY METHODS

The connection of the PO method and the GO method could be obtained via the HFA technique. On invoking the HFA technique for Equation (24), one could obtain that the leading term of the PO scattered field corresponds to the GO ray field at the specular reflection point in Equation (5). As is known, the GTD method serves as the correction of the GO method with the consideration of the edge diffracted wave fields. And UTD method comes from the uniform asymptotic approximation of the radiation integrals from the wedge diffraction problems. When the observation point lies outside of the incident and reflection shadow boundaries of the wedge diffraction problem, the UTD diffraction coefficient in Equation (20) could reduce to the GTD coefficient in Equation (19).

The PTD current is the summation of the PO approximation current and the edge diffracted wave approximation current. The scattered fields from the PTD method are expressed as the radiation integrals. When the radiation integrals are approximated in the asymptotic way, the results are similar to the wave fields obtained from the GTD method. Furthermore, when the radiation integrals are approximated in the uniform asymptotic fashion, the scattered fields from the UTD method result. With respect to the computational workload, the scattered fields from the GO, GTD and UTD methods are frequency independent. However, the calculations of the scattered fields from the PO and PTD methods via the direction numerical integration are frequency dependent. With respect to the accuracy, on invoking the direction numerical integration method for the scattered fields from the PO and PTD methods, the generated results are more accurate than those generated from the GO, GTD and UTD methods.

Recently, progress is made on the fast evaluation of the high frequency scattered fields by the NSDP method [47–50]. The efficient NSDP method is adopted to calculate the scattered fields from the PO method and the ILDC method in the following Section 10.

10. THE NUMERICAL REPRODUCIBILITY

The numerical reproducibility of the PO scattered fields by the NSDP method could be given as follows:
Step 1. We identify three types of quadratic surfaces, which are parabolic, hyperbolic and saddle.
Step 2. We formulate the PO scattered field formulations on the assembled quadratic triangular patches.
Step 3. We implement the affine transformation and transform the PO surface integral on each quadratic triangular patch to its canonical form.
Step 4. We reduce the PO surface integral to three highly oscillatory line integrals on each quadratic triangular patch.
Step 5. We find the phase formulations of the PO integrands from the quadratic surfaces.
Step 6. From the obtained phase formulations, we find all kinds of NSDPs on the complex plane.
Step 7. We formulate all cases of the Stokes' lines on the complex plane.
Step 8. From the Cauchy's integral theorem, we obtain the PO scattered fields formulations via the NSDPs on the complex plane.
Step 9. We calculate the radar cross section of the PO scattered fields with frequency independent computational workload and error controllable accuracy.
The numerical reproducibility of the high frequency scattered fields from the convex scatterers by the ILDC and NSDP methods could be expressed as follows:
Step 1. We find the curvature of the convex scatterers.
Step 2. We find the geodesic curve of the convex scatterers and derive the formulations of the Fock currents.
Step 3. We calculate the Fock currents by the hybrid fast solver, that is, the hybridization of the high frequency asymptotic (HFA) method and the NSDP method.
Step 4. From the Fock current, we calculate the high frequency scattered fields along the incremental length differential direction.
Step 5. With the ILDC technique, we calculate the radar cross section (RCS) of the high frequency scattered fields from the convex scatterers.
Step 6. In order to study the wave physics, we separate the PO scattered fields and the diffracted wave fields from the convex scatterers by the ILDC technique.

11. NUMERICAL RESULTS BY THE NSDP METHOD

To demonstrate the strength of the proposed NSDP method, we consider the scattered fields from the PO method and the ILDC method in this section. We first apply the NSDP method to analyze the PO scattered field on the parabolic surface, as demonstrated in Figure 8(a). The NSDP method is adopted for calculating the bistatic case PO scattered fields in Equation (26). The parameters: the frequency $k \in [10, 500]$, the incident wave propagates along $\hat{\mathbf{r}}^{(i)} = \left[0.5, 0.5, -\sqrt{2}/2\right]$ direction, the observation point is set along the unit direction $\hat{\mathbf{r}} = \left[\sqrt{2}/4, \sqrt{6}/4, \sqrt{2}/2\right]$, and the incident electric wave has polarization amplitude $\mathbf{E}_0{}^{(i)} = \left[-\sqrt{2}/2, \sqrt{2}/2, 0\right]$ with $\mathbf{E}_0{}^{(i)} \cdot \hat{\mathbf{r}}^{(i)} = 0$. On invoking the NSDP method, Figures 10–11 demonstrate the error-controllable accuracy and frequency-independent workload for calculating the bistatic PO scattered fields.

To show the accuracy of the NSDP method for calculating $\mathbf{E}_s(\mathbf{r})$ on the parabolic patch, Figure 12 presents the comparison of relative errors between the NSDP and HFA methods relative to the brute force method [32]. It can be seen that the NSDP method can significantly improve the accuracy of $\mathbf{E}_s(\mathbf{r})$ by around two digits $\left(10^{-2}\right)$ when the working frequency k is not extremely large.

The second numerical example is the application of the NSDP method for the calculation of the scattered fields with the ILDC technique for the 3-D convex scatterer. The incident plane wave with x-polarized direction is impinging on the electrically large convex sphere in the z-direction. The NSDP

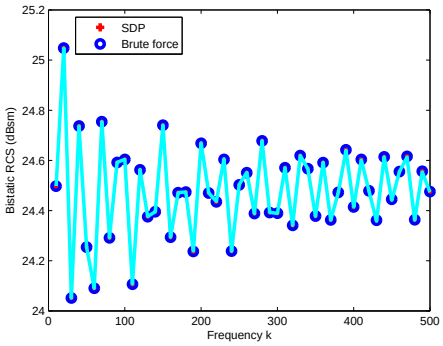

Figure 10. Comparisons of the RCS (dBsm unit) values of the PO scattered field (26) by the NSDP method and the brute force method.

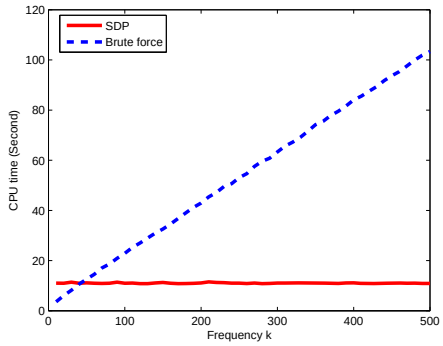

Figure 11. Comparisons of the CPU time (second unit) for the PO scattered field (26) by using the NSDP method and the brute force method.

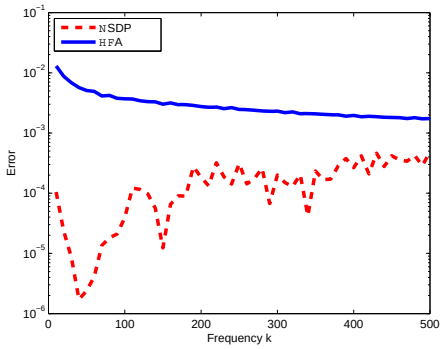

Figure 12. Red line: The relative error of $\mathbf{E}_s(\mathbf{r})$ produced by using the NSDP method relative to the brute force method. Blue line: The relative error of $\mathbf{E}_s(\mathbf{r})$ produced by using the HFA method relative to the brute force method.

technique is adopted to evaluate the Fock current from the convex scatterer [52]. With the wave physics viewpoint, the Fock current contains rich physics from the convex scatterer, including the PO current in the lit region, the NU-Fock current in the transition region and the deep shadow regions, respectively. In this sense, the scattered fields from the uniform Fock current shall greatly enhance the accuracy of those obtained by the PO current alone. In Figure 13, the effect of the wave physics of the convex scatterer is clearly demonstrated. The scattered field from the summation of the PO current and the NU-Fock current in the lit region is represented by the dashed blue line, which clearly demonstrates the accuracy enhancement from the PO scattered fields. However, compared to the scattered field results

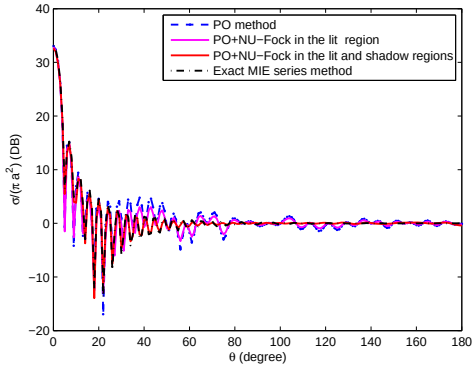

Figure 13. The far scattered fields from the 3-D conducting sphere are produced by the PO approximation current, the summation of the PO current and the NU-Fock currents in the scatterer's lit and shadow regions, and the Mie series method, respectively. The product of the wave frequency and the radius of the sphere has the value $kR = 45$.

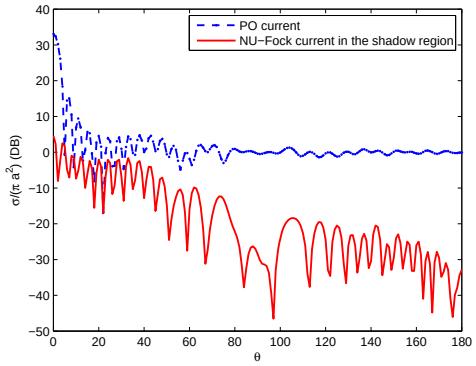

Figure 14. Comparison of the contributions of the PO scattered fields and the wave fields from the NU-Fock current in the shadow region of the sphere, with $kR = 45$.

from the uniform Fock current in the lit and shadow regions, the NU-Fock current in the lit region still lose the accuracy. To demonstrate the effect of the NU-Fock current in the shadow region, the contributions of the creeping wave fields from the NU-Fock current in the shadow region are shown in Figure 14. In summary, on invoking the ILDC technique and the NSDP method for the 3-D convex scatterer, the scattered fields from the Fock currents gain high accuracy and could even agree well with the Mie series solution.

11.1. Accuracy Improvements of the High Frequency Methods

As shown in Figure 12, compared with the conventional HFA method, the NSDP method could significantly improve the accuracy of the PO scattered fields in Equation (26) with two digits. On invoking the NSDP method, the PO surface integral is exactly expressed as some contour integrals in Equation (41) with exponentially decaying integrand on the complex plane. The only approximation process is the Gauss-Laguerre quadrature rule for the contour integrals in Equation (41). And this approximation process could gain high accuracy results. Meanwhile, on adopting the HFA method with the asymptotic expansion, the surface integrals are expressed as several leading terms. This is the reason that the high frequency PO scattered fields from the NSDP method could improve the accuracy from the HFA method. Furthermore, we adopt the NSDP method together with the ILDC technique for calculating the diffracted fields from the electrically large and convex scatterers. On invoking the NSDP method, the high frequency scattered fields from the ILDC technique could significantly enhance the accuracies from the PO scattered fields, which is shown in Figure 13.

11.2. Discussions on the Numerical Results from the High Frequency Methods

In Figure 10, the PO scattered fields results from the quadratic parabolic surfaces are demonstrated by the NSDP method and the brute force method. From the confirmations of the PO scattered fields results by the brute force method, the NSDP method could generate error controllable results. With the respect to the computational workload, Figure 11 depicts that the NSDP method could generate the frequency independent workload on the calculation of the PO scattered field. Moreover, with respect to the accuracy of the PO scattered fields, Figure 12 depicts that the NSDP method could significantly yield two digits accuracy. The reason is that less approximation of the NSDP method is done than the HFA method.

Figures 13–14 demonstrate the high frequency scattered field results from the convex scatterers by the ILDC method. As shown in Figure 13, the results of the high frequency scattered fields from the Fock current agree well with those from the exact MIE series solutions. Meanwhile, the PO scattered fields loose the accuracy in the shadow and transition regions of the considered scatterers.

12. CONCLUSIONS

In this work, we give a review of the recent important high frequency techniques. The high frequency techniques could be classified into the current based and ray based methods. Various high frequency methods were developed over last decades to calculate the scattered fields. To compute the high frequency scattered fields, the NSDP method provides an efficient way. On invoking the NSDP method, the radiation integrals from the PO and ILDC methods could be transformed to some smooth kernels on the complex plane. By adopting the Gauss-Laguerre quadrature rule, the NSDP method provides the frequency independent approach to evaluate these radiation integrals. Furthermore, the rich high frequency wave physics from the edge and convex body are covered in this review paper. Finally, the improvement of the accuracy and speed of existing high-frequency techniques requires further research in this area.

ACKNOWLEDGMENT

This work was supported in part by NSFC 61401103, in part by NSF-SH Grant 14ZR1402400, in part by the talent recruitment under Grant IDH1207001 by Fudan University, in part by the State Key Laboratory of Millimeter Waves Grant K201505, in part by Innovation Fund of Petro-China 2014D-5006-0301, in part by SINOPEC Key Laboratory of Geophysics 33550006-14-FW2099-0034, in part by the Research Grants Council of Hong Kong (GRF 712612 and 711511), in part by US AR120018 contracted through UTAR, and in part by USA NSF CCF Award 1218552.

REFERENCES

1. Maxwell, J. C., "A dynamical theory of the electromagnetic field," *Philosophical Transactions of the Royal Society of London*, 459–512, 1865.
2. Heaviside, O., *Electromagnetic Theory*, Vol. 3, Cosimo, Inc., 2008.
3. Chew, W. C., *Waves and Fields in Inhomogeneous Media*, IEEE Press, New York, 1995.
4. Kong, J. A., *Electromagnetic Wave Theory*, Wiley-Interscience, New York, 1990.
5. Knott, E. F., J. F. Shaeffer, and M. T. Tuley, *Radar Cross Section*, Artech House, Norwood, 1993.
6. Balanis, C. A., *Antenna Theory: Analysis and Design*, Wiley, John Wiley-Sons, 2012.
7. Datta, S., *Quantum Transport: Atom to Transistor*, Cambridge University Press, 2005.
8. Cai, W., *Computational Methods for Electromagnetic Phenomena: Electrostatics in Solvation, Scattering, and Electron Transport*, Cambridge University Press, Cambridge, 2013.
9. Garrison, J. and R. Chiao, *Quantum Optics*, Oxford University Press, USA, 2014.
10. Tang, L., J. A. Kong, and B. Shin, *Theory of Microwave Remote Sensing*, John Wiley, New York, 1985.

11. Jin, Y. Q., *Electromagnetic Scattering Modelling for Quantitative Remote Sensing*, World Science Press, Singapore, 2000.
12. Harrington, R. F., *Field Computation by Moment Method*, Macmillan, New York, 1968.
13. Jin, J. M., *The Finite Element Method in Electromagnetics*, 3rd edition, Wiley-IEEE Press, Hoboken, 2014.
14. Taflove, A. and S. C. Hagness, *Computational Electrodynamics: The Finite-difference Time-domain Method*, 3rd edition, Artech House, Boston, 2015.
15. Song, J. M., C. C. Lu, and W. C. Chew, "Multilevel fast multipole algorithm for electromagnetic scattering by large complex objects," *IEEE Trans. Antennas Propag.*, Vol. 45, No. 10, 1488–1493, Oct. 1997.
16. Chew, W. C., J. M. Jin, E. Michielssen, and J. M. Song, *Fast and Efficient Algorithms in Computational Electromagnetics*, Artech House, Boston, 2001.
17. Macdonald, H. M., "The effect produced by an obstacle on a train of electric waves," *Phil. Trans. Royal Soc. London, Series A, Math. Phys. Sci.*, Vol. 212, 299–337, 1913.
18. Ufimtsev, P. Y., *Backscatter*, John Wiley and Sons, New York, 2005.
19. Ufimtsev, P. Y., *Fundamentals of the Physical Theory of Diffraction*, John Wiley and Sons, Inc., New York, 2007.
20. Mitzner, K. M., *Incremental Length Diffraction Coefficients*, Tech. Rep. No. AFAL-TR-73-296, 1974.
21. Shore, R. A. and A. D. Yaghjian, "Incremental diffraction coefficients for planar surfaces," *IEEE Trans. Antennas Propag.*, Vol. 36, 55–70, 1988.
22. Hansen, T. B. and R. A. Shore, "Incremental length diffraction coefficients for the shadow boundary of a convex cylinder," *IEEE Trans. Antennas Propag.*, Vol. 46, No. 10, 1458–1466, 1998.
23. Yaghjian, A. D., R. A. Shore, and M. B. Woodworth, "Shadow boundary incremental length diffraction coefficients for perfectly conducting smooth, convex surfaces," *Radio Sci.*, Vol. 31, No. 12, 1681–1695, 1996.
24. Keller, J. B., "Geometrical theory of diffraction," *J. Opt. Soc. Am.*, Vol. 52, No. 2, 116–130, 1962.
25. James, G. L., *Geometrical Theory of Diffraction for Electromagnetic Waves*, Peregrinus, Stevenage, 1980.
26. Kouyoumjian, R. G. and P. H. Pathak, "A uniform geometrical theory of diffraction for an edge in a perfectly conducting surface," *Proc. IEEE*, Vol. 62, No. 11, 1448–1461, 1974.
27. Lee, S. W. and G. A. Deschamps, "A uniform asymptotic theory of electromagnetic diffraction by a curved wedge," *IEEE Trans. Antennas Propag.*, Vol. 24, No. 1, 25–34, 1976.
28. Kouyoumjian, R. G., "Asymptotic high-frequency methods," *Proc. IEEE*, Vol. 53, No. 8, 864–876, 1965.
29. Pathak, P. H., "High-frequency techniques for antenna analysis," *Proc. IEEE*, Vol. 80, No. 1, 44–65, 1992.
30. Borovikov, V. A., *Uniform Stationary Phase Method*, Institution of Electrical Engineers, London, 1994.
31. Conde, O. M., J. Pérez, and M. F. Cátedra, "Stationary phase method application for the analysis of radiation of complex 3-D conducting structures," *IEEE Trans. Antennas Propag.*, Vol. 49, No. 5, 724–731, 2001.
32. Carluccio, G., M. Albani, and P. H. Pathak, "Uniform asymptotic evaluation of surface integrals with polygonal integration domains in terms of UTD transition functions," *IEEE Trans. Antennas Propag.*, Vol. 58, No. 4, 1155–1163, 2010.
33. Sommerfeld, A., "Mathematische theorie der diffraction," *Mathematische Annalen.*, Vol. 47, No. 319, 317–374, 1896.
34. Fock, V. A., "The distributions of currents induced by a plane wave on the surface of a conductor," *J. Phys.*, Vol. 10, 130–136, 1946.
35. Kline, M., *Mathematical Theory of Optics*, Brown University Notes, Providence, RI, 1944.

36. Ling, H., R. C. Chou, and S. W. Lee, "Shooting and bouncing rays: Calculating the RCS of an arbitrarily shaped cavity," *IEEE Trans. Antennas Propag.*, Vol. 37, No. 2, 194–205, 1989.
37. Lee, S. W. and R. Mittra, "Fourier transform of a polygonal shape function and its application in electromagnetics," *IEEE Trans. Antennas Propag.*, Vol. 31, No. 1, 99–103, 1983.
38. Gordon, W. B., "High-frequency approximations to the physical optics scattering integral," *IEEE Trans. Antennas Propag.*, Vol. 42, No. 3, 427–432, 1994.
39. Engquist, B., E. Fatemi, and S. Osher, "Numerical solution of the high frequency asymptotic expansion for the scalar wave equation," *J. Comput. Phys.*, Vol. 120, No. 1, 145–155, Aug. 1995.
40. Engquist, B. and O. Runborg, "Computational high frequency wave propagation," *Acta Numerica*, Vol. 12, 181–266, 2003.
41. Wong, R., *Asymptotic Approximations of Integrals*, SIAM, New York, 2001.
42. Abramowitz, M. and I. A. Stegun, *Handbook of Mathematical Functions*, MA, Dover, Norwood, 1972.
43. Josef, S. and B. Roland, *Introduction to Numerical Analysis*, Springer-Verlag, New York, 1980.
44. Asheim, A. and D. Huybrechs, "Asymptotic analysis of numerical steepest descent with path approximations," *Found. Comput. Math.*, Vol. 10, No. 6, 647–671, 2010.
45. Bondia, F. V., M. Ferrando-Bataller, and A. Valero-Nogueira, "A new fast physical optics for smooth surfaces by means of a numerical theory of diffraction," *IEEE Trans. Antennas Propag.*, Vol. 58, No. 3, 773–789, 2010.
46. Zhang, J., B. Xu, and T. J. Cui, "An alternative treatment of saddle stationary phase points in physical optics for smooth surfaces," *IEEE Trans. Antennas Propag.*, Vol. 62, No. 2, 986–991, 2014.
47. Wu, Y., L. J. Jiang, and W. C. Chew, "An efficient method for computing highly oscillatory physical optics integral," *Progress In Electromagnetics Research*, Vol. 127, 211–257, 2012.
48. Wu, Y. M., L. J. Jiang, and W. C. Chew, "An efficient method for computing highly oscillatory physical optics integral," *Symp. on Antennas and Propag. (IEEE APS12)*, 2012.
49. Wu, Y. M., L. J. Jiang, W. E. I. Sha, and W. C. Chew, "The numerical steepest descent path method for calculating physical optics integrals on smooth conducting surfaces," *IEEE Trans. Antennas Propag.*, Vol. 61, No. 8, 4183–4193, 2013.
50. Wu, Y. M., L. J. Jiang, and W. C. Chew, "Computing highly oscillatory physical optics integral on the polygonal domain by an efficient numerical steepest descent path method," *J. Comput. Phys.*, Vol. 236, 408–425, 2013.
51. Wu, Y. M., L. Jiang, and W. C. Chew, "The contour deformation method for calculating the high frequency scattered fields by the Fock current on the surface of the 3-D convex cylinder," *Symp. on Antennas and Propag. (IEEE APS14)*, Jul. 2014.
52. Wu, Y. M., L. J. Jiang, W. C. Chew, and Y. Q. Jin, "The contour deformation method for calculating the high frequency scattered field by the Fock current on the surface of the 3-D convex cylinder," *IEEE Trans. Antennas Propag.*, Vol. 63, No. 5, 2180–2190, 2015.
53. Perrey-Debain, E., J. Trevelyan, and P. Bettess, "Wave boundary elements: A theoretical overview presenting applications in scattering of short waves," *Eng. Anal. Bound. Elem.*, Vol. 28, 131–141, 2004.
54. Engquist, B., A. Fokas, E. Hairer, and A. Iserles, *Highly Oscillatory Problems*, London Mathematical Society Lecture Note Series, Cambridge University Press, 2009.
55. Chandler, S. N. and S. Langdon, *Acoustic Scattering: High Frequency Boundary Element Methods and Unified Transform Methods*, SIAM, New York, 2015.
56. Cheng, H., W. Y. Crutchfield, Z. Gimbutas, L. F. Greengard, J. F. Ethridge, J. Huang, V. Rokhlin, N. Yarvin, and J. Zhao, "A wideband fast multipole method for the Helmholtz equation in three dimensions," *J. Comput. Phys.*, Vol. 216, No. 1, 300–325, 2006.
57. Bruno, O. P., *Fast, High-order, High-frequency Integral Methods for Computational Acoustics and Electromagnetics*, Springer, Berlin Heidelberg, 2003.
58. Umul, Y. Z., "Rigorous expressions for the equivalent edge currents," *Progress In Electromagnetics Research B*, Vol. 15, 77–94, 2009.

59. Michaeli, A., "Equivalent edge currents for arbitrary aspects of observation," *IEEE Trans. Antennas Propag.*, Vol. 32, 252–258, 1984.
60. Chou, H. T., P. H. Pathak, and P. R. Rousseau, "TD-UTD solutions for the transient radiation and surface fields of pulsed antennas placed on PEC smooth convex surfaces," *IEEE Trans. Antennas Propag.*, Vol. 59, No. 5, 1626–1637, 2011.
61. Johansen, P. M., "Time-domain version of the physical theory of diffraction," *IEEE Trans. Antennas Propag.*, Vol. 47, 261–270, 1999.